Journal of Zhejiang University-SCIENCE A (Applied Physics & Engineering)
ISSN 1673-565X (Print); ISSN 1862-1775 (Online)
www.jzus.zju.edu.cn; www.springerlink.com
E-mail: jzus@zju.edu.cn

# Large eddy simulation of unsteady aerodynamic behavior of long-span vaulted roofs*

Wei DING[†1,2], Yasushi UEMATSU[3]
([1]School of Mechanics and Civil Engineering, China University of Mining and Technology, Xuzhou 221116, China)
([2]Jiangsu Collaborative Innovation Center for Building Energy Saving Construction Technology, Xuzhou 221116, China)
([3]Department of Architecture & Building Science, Tohoku University, Aoba-ku, Sendai 980-8579, Japan)
[†]E-mail: emily_dw@163.com

Received Oct. 21, 2016;  Revision accepted Feb. 21, 2017;  Crosschecked Sept. 7, 2017

**Abstract:** This paper discusses the unsteady aerodynamic behavior of long-span vaulted roofs. First, a forced vibration test in a turbulent boundary layer is conducted in a wind tunnel. The models are force vibrated in the first anti-symmetric mode to investigate the effects of wind speed, rise/span ratio, and the amplitude and frequency of forced vibration on the distributions of wind pressures and unsteady aerodynamic forces. Then, a large eddy simulation (LES) is carried out to clarify the physical mechanism of wind-roof interaction as well as to investigate the influences of a roof's vibration on the flow field around the roof. From the results of the wind tunnel experiment and the LES, we discuss the characteristics of unsteady aerodynamic forces on a long-span vaulted roof over a wide range of the reduced frequency of vibration. The effect of unsteady aerodynamic forces on the dynamic response of the roof is also discussed. A comparison between the wind tunnel experiment and the LES indicates that the LES can be used effectively to evaluate the unsteady aerodynamic behavior.

**Key words:** Long-span vaulted roof; Unsteady aerodynamic behavior; Large eddy simulation (LES); Wind tunnel experiment; Forced vibration test
http://dx.doi.org/10.1631/jzus.A1600691   **CLC number:** TU318.1

## 1 Introduction

Many long-span structures with vaulted roofs, such as gymnasiums or airport hangars, have been constructed in that way because they have aerodynamically efficient shapes compared with regular rectangular buildings. Such structures are generally vulnerable to the dynamic wind actions because of low damping and frequency (Blackmore and Tsokri, 2006; Chen *et al*., 2011; Natalini *et al*., 2013; Wu *et al*., 2015). The wind-structure interaction induces unsteady aerodynamic forces, or motion-induced wind forces, which may affect the wind-induced response significantly (Yang *et al*., 2010; Chen *et al*., 2015). Therefore, the unsteady aerodynamic force is an important consideration in the design of long-span vaulted roofs. Uematsu and Uchiyama (1982) conducted a series of wind tunnel tests using elastic models of a one-way type of suspended roof. The mechanism of the wind-induced vibrations and the effect of wind-roof interaction on the dynamic response were discussed. Daw and Davenport (1989) carried out a forced vibration test on a semi-circular roof to investigate the dependence of unsteady aerodynamic forces on the turbulence intensity, wind speed, vibration amplitude, and geometric details of the roof. Ohkuma and Marukawa (1990) investigated the mechanism of aeroelastic instability of long-span

---

* Project supported by the Foundation of Jiangsu Collaborative Innovation Center for Building Energy Saving Construction Technology for Young Teachers (No. SJXTQ1515), China
ORCID: Wei DING, http://orcid.org/0000-0002-5556-2364

flat roofs using a forced vibration test in a wind tunnel. At present, long-span vaulted roofs are universally constructed. However, there is insufficient research on unsteady aerodynamic forces on long-span vaulted roofs, and the characteristics of unsteady aerodynamic forces are not well understood.

The purpose of this study is to describe the detailed unsteady aerodynamic behavior of long-span vaulted roofs to improve wind-resistant design. A forced vibration test is carried out in a turbulent boundary layer to investigate the effects of wind speed, rise/span ratio, and the amplitude and frequency of the forced vibration on the wind pressure and unsteady aerodynamic forces. Because of the limitation of the forced vibration equipment used in the wind tunnel test, the models cannot be vibrated at high vibration frequencies. Therefore, we conduct a large eddy simulation (LES) to examine the influences of a roof's vibration on the wind pressure over a wider range of forced vibration frequency. The focus is on the unsteady aerodynamic forces in order to discuss the effect of wind-roof interaction on the dynamic response. The characteristics are investigated over a wider range of the reduced frequency of vibration than using wind tunnel alone. In addition, the LES is carried out to investigate the effect of a roof's vibration on the flow field around the roof to clarify the physical mechanism of wind-roof interaction.

## 2 Wind tunnel experiments

### 2.1 Experimental apparatus and procedures

The wind tunnel experiments were carried out in an Eiffel-type wind tunnel at Tohoku University, Japan. The working section of wind tunnel is 6.5 m in length and 1.0 m×1.4 m in cross-section. A turbulent boundary layer with a power-law exponent of $\alpha$=0.23 for the mean wind speed profile was simulated using a set of turbulence generating spires installed at the entrance of the working section and a number of roughness blocks distributed on the floor (Fig. 1). The profiles of the mean wind speed and turbulence intensity are shown in Fig. 2. The reference wind speed was measured at a height of $Z_G$=500 mm. The longitudinal velocity spectrum was generally consistent with the so-called Karman type spectrum.

**Fig. 1 Distribution of roughness blocks and spires**

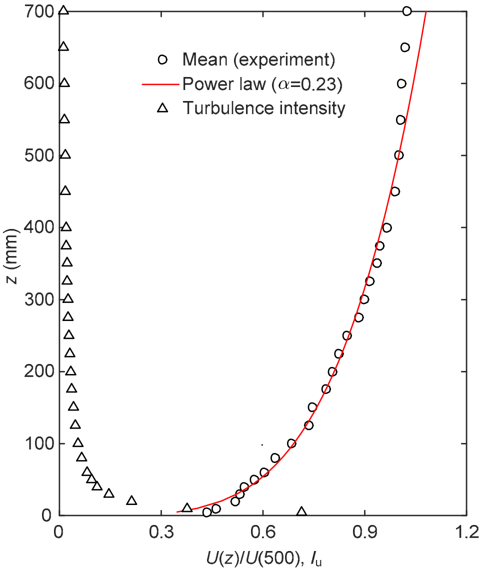

**Fig. 2 Profiles of the mean wind speed $U$ and turbulence intensity $I_u$**

Fig. 3a shows the geometry of the experimental model. The model is made of 0.8 mm thick polyester film. Roofs with rise/span ratio ($r/L$) of 0.15 and 0.20 are tested. $s$ represents the circumferential coordinate along the roof, and $R_s$ is the total length of the roof. Fig. 4 shows the forced vibration equipment that makes the roof vibrate in the first anti-symmetric mode (Fig. 3b). A pair of end plates is set to make the flow two-dimensional. Each model has 12 pressure taps of 1 mm diameter uniformly distributed along the roof's centreline. The pressure taps are connected to pressure transducers in parallel via 80 cm lengths of flexible vinyl tubing. The tubing effects are numerically compensated using the gain and phase-shift characteristics of the pressure measuring system, which includes tubes, pressure transducers, and low-pass filters of 300 Hz. The wind pressures acting on the vibrating roof are measured and sampled simultaneously at a rate of 500 Hz for a period of approximately 60 s. The experimental parameters involved in the experiments are summarized in Table 1.

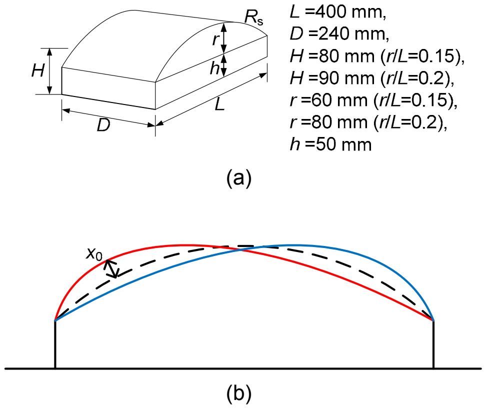

(a)

(b)

**Fig. 3 Geometry of the experimental model**

(a) Experimental model; (b) First anti-symmetric mode of vibration. $H$ is the mean roof height

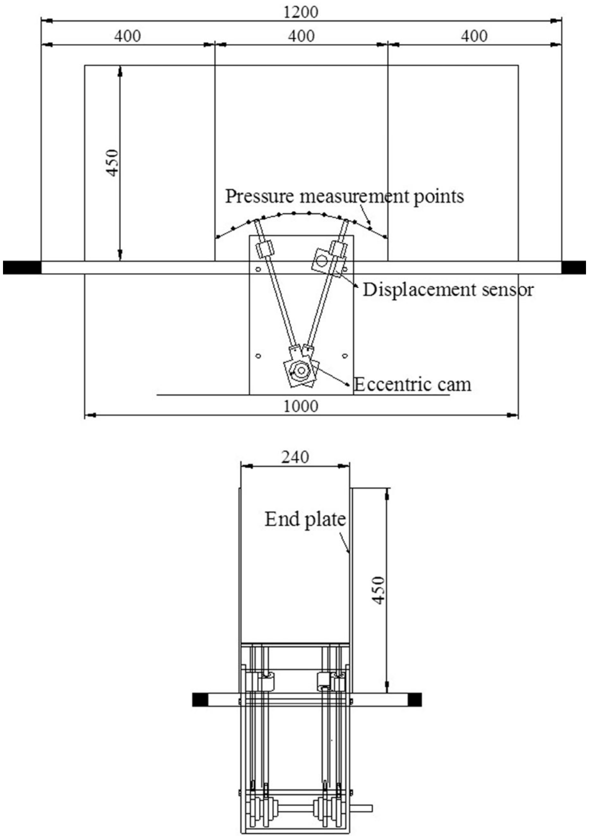

**Fig. 4 Experimental setup of the forced vibration test (unit: mm)**

**Table 1 Parameters of experiment**

| Parameter | Value |
|---|---|
| Rise/span ratio, $r/L$ | 0.15, 0.20 |
| Wind speed, $U_H$ (m/s) | 5.0, 7.0, 10.0 |
| Forced vibration amplitude, $x_0$ (mm) | 1.0, 2.5, 4.0 |
| Forced vibration frequency, $f_m$ (Hz) | 5–25 (interval 1 Hz) |

## 2.2 Results of wind tunnel experiments

### 2.2.1 Characteristics of wind pressures on the vibrating roof

The wind pressure coefficient at tap $i$ on the model surface is defined in terms of the velocity pressure $q_H$ at the mean roof height $H$. Fig. 5 shows the distributions of the mean wind pressure coefficients $Cp_{mean}$ and root mean square (RMS) fluctuating wind pressure coefficients $Cp_{rms}$ for various wind speeds, vibration amplitudes, and forced vibration frequencies. It is found that the $Cp_{mean}$ distribution is minutely influenced by wind speed, vibration amplitude, and forced vibration frequency within the limits of the present experiment. On the other hand, the value of $Cp_{rms}$ increases with increasing frequency and amplitude of forced vibration. Such an increase in $Cp_{rms}$ may be due to an increase in the deflection velocity of the roof.

### 2.2.2 Characteristics of unsteady aerodynamic forces

Unsteady aerodynamic forces are caused by a wind-roof interaction. The equation of motion for the $j$th generalized displacement $x_j(t)$ of the roof including the unsteady aerodynamic forces can be given by the following equations:

$$\ddot{x}(t)+2\zeta_j\omega_j\dot{x}_j(t)+\omega_j^2x_j(t)=F_j(t)/M_j, \quad (1)$$

$$F_j(t)=F_{Wj}(t)+F_{Aj}(x_j,\dot{x}_j,\ddot{x}_j,\cdots), \quad (2)$$

where $M_j$ is the generalized mass, $\omega_j$ is the natural circular frequency, $\zeta_j$ is the critical damping ratio, and $F_j$ is the generalized force. $F_{Wj}$ represents the fluctuating wind force due to the oncoming flow and wake instability, while $F_{Aj}$ is the unsteady aerodynamic force.

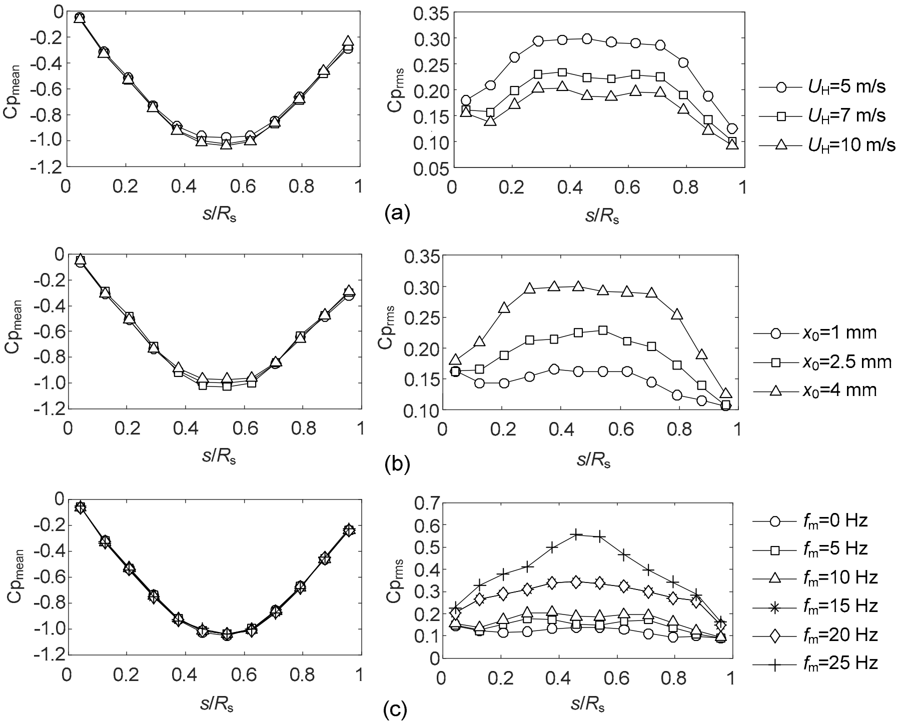

**Fig. 5 Variation of mean and fluctuating wind pressure coefficients for various wind velocities ($f_m$=10 Hz, $x_0$=4 mm) (a), forced vibration amplitudes ($f_m$=10 Hz, $U_H$=5 m/s) (b), and forced vibration frequencies ($x_0$=4 mm, $U_H$=10 m/s) (c) ($r/L$=0.15)**

In the case of the forced vibration test, a steady vibration in the first anti-symmetric mode represented by a sine curve is applied to the roof (Fig. 3b). The unsteady aerodynamic force $F_{Aj}$ (here $j$=1) may be obtained from Eq. (3) using the Fourier series at the frequency $f_m$ of the forced vibration:

$$F_{Aj}(t)=F_{Rj}\cos(2\pi f_m t)-F_{Ij}\sin(2\pi f_m t), \tag{3}$$

$$F_{Rj}=\frac{1}{T}\int_{-T}^{T}F_j(t)\cos(2\pi f_m t)\mathrm{d}t, \tag{4}$$

$$F_{Ij}=\frac{1}{T}\int_{-T}^{T}F_j(t)\sin(2\pi f_m t)\mathrm{d}t, \tag{5}$$

where $F_{Rj}$ and $F_{Ij}$ are the in-phase and out-of-phase components of the unsteady aerodynamic force, respectively.

We use the aerodynamic stiffness coefficient $a_{Kj}$ and aerodynamic damping coefficient $a_{Cj}$ to investigate the characteristics of the unsteady aerodynamic forces acting on a vibrating long-span vaulted roof, which are given by the following equations (Katagiri et al., 2001):

$$\begin{aligned}a_{Kj}&=\frac{F_{Rj}(f_m)}{q_H A_s(x_0/L)}\\&=\frac{1}{q_H A_s(x_0/L)}\frac{2}{T}\int_0^T F_j(t)\cos(2\pi f_m t)\mathrm{d}t,\end{aligned} \tag{6}$$

$$\begin{aligned}a_{Cj}&=\frac{F_{Ij}(f_m)}{q_H A_s(x_0/L)}\\&=\frac{1}{q_H A_s(x_0/L)}\frac{2}{T}\int_0^T F_j(t)\sin(2\pi f_m t)\mathrm{d}t,\end{aligned} \tag{7}$$

where $F_{Rj}$ is the in-phase component with the generalized displacement represented as the aerodynamic stiffness term, $F_{Ij}$ is the out-of-phase component with velocity represented as the aerodynamic damping term, $q_H$ is the velocity pressure at the mean roof height $H$, $A_s$ is the roof area, $T$ is the vibration period, and $f_m^*$ is the reduced frequency of vibration, defined by $f_m H/U_H$, with $U_H$ being the mean wind speed at the mean roof height $H$.

The generalized force $F_j$ may be described in terms of the external and internal pressures, $p_e$ and $p_i$, as shown in Eq. (8) and Fig. 6.

$$F_j\left(t\right)=\int_0^{R_s}\left[p_{ej}\left(s,t\right)-p_{ij}\left(s,t\right)\right]\phi_j\left(s\right)\mathrm{d}s. \tag{8}$$

In this study, the first anti-symmetric mode is considered ($j$=1) and $\phi_{j=1}(s)$ is represented by Eq. (9). The internal pressure $p_i$ is ignored because the first anti-symmetric mode causes no change of internal volume. The data of external pressures $p_e$ can be obtained from the wind tunnel tests. Therefore, the generalized force can be defined by Eq. (10).

$$\phi_{j=1}(s)=\sin\left(2\pi\frac{s}{R_s}\right), \tag{9}$$

$$F_{j=1}\left(t\right)=\int_0^{R_s}p_e\left(s,t\right)\sin\left(2\pi\frac{s}{R_s}\right)\mathrm{d}s. \tag{10}$$

Figs. 7a and 7b show the variation of the aerodynamic stiffness coefficient $a_K$ with $f_m^*$ for various wind speeds and vibration amplitudes; the rise/span ratio is 0.15. The value of $a_K$ generally increases with the increase of $f_m^*$. As the reduced frequency of vibration decreases, the value of $a_K$ approaches the quasi-steady value (represented by the dashed line in the figure). Similar results were observed for $r/L$=0.20. This feature is consistent with the result obtained by Daw and Davenport (1989). The value of $a_K$ is generally positive, which may reduce the total stiffness of the structural system, resulting in a lower natural frequency.

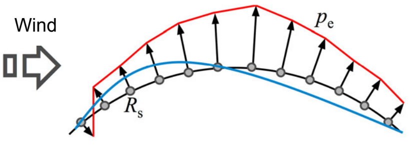

**Fig. 6 The first anti-symmetric mode of vibration**

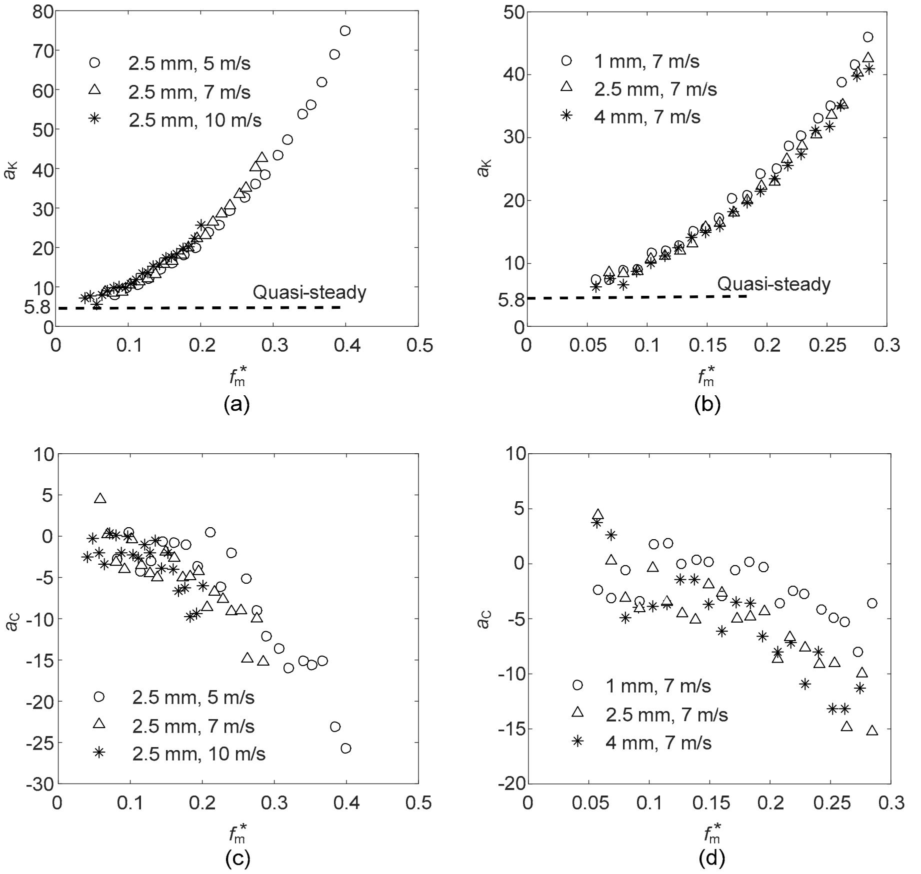

**Fig. 7 Variation of aerodynamic stiffness coefficient $a_K$ and aerodynamic damping coefficient $a_C$ with reduced frequency of vibration $f_m^*$ ($r/L$=0.15)**

(a) Dependence on wind velocity ($a_K$-$f_m^*$); (b) Dependence on amplitude of forced vibration ($a_K$-$f_m^*$); (c) Dependence on wind velocity ($a_C$-$f_m^*$); (d) Dependence on amplitude of forced vibration ($a_C$-$f_m^*$)

Figs. 7c and 7d show the variation of aerodynamic damping coefficient $a_C$ with $f_m^*$ for various wind speeds and vibration amplitudes; the rise/span ratio is also 0.15. The values of $a_C$ are generally negative except for small $f_m^*$ values, which may result in an increase in the total damping of the structural system. The magnitude of $a_C$ increases as the $f_m^*$ value increases. Similar results were observed for $r/L$=0.20. Within the limits of the present experiments, it can be seen that the values of the aerodynamic stiffness and damping coefficients $a_K$ and $a_C$ are mainly dependent on the reduced frequency of vibration $f_m^*$. Compared with the effects of $f_m^*$, the effects of wind speed, rise/span ratio, and vibration amplitude on the aerodynamic stiffness and damping coefficients $a_K$ and $a_C$ are small.

## 3 Large eddy simulation

Because the wind tunnel experiment is limited, an LES is carried out to reproduce the wind tunnel experiment. We use the results of the LES to investigate the influences of a roof's vibration on the wind pressure and flow field around a vibrating roof. The characteristics of unsteady aerodynamic forces in a wider range of reduced frequency of vibration are also investigated.

### 3.1 Computational profile

The simulation is carried out using a computational fluid dynamic (CFD) software 'STAR-CD', in which LES with the Smagorinsky sub-gird model (Smagorinsky constant $C_s$=0.12) is used. The vaulted roof model is forced to vibrate in the first anti-symmetric mode as shown in Fig 3b. Table 2 summarizes the values of parameters discussed in this study. In order to discuss the effect of geometric shape on wind-roof interaction, the rise/span ratio is changed from 0.15 to 0.25. The amplitude $x_0$ of vibration is fixed to 4.0 mm (i.e., $x_0/L$=1/100). In this study, based on the assumptions of the mean roof height for real structure $H_{\_r}$=20 m; the wind speed at mean roof height $U_{H\_r}$=20–40 m/s; the natural frequency $f_s$=0.4–2.5 Hz. We calculated the reduced frequency for real roof $f_{\_r}^*$=0.2–2.5, as shown in Table 3. In order to satisfy the similarity principle of real long-span roofs $f_m^*=f_{\_r}^*$ ($f_m^*$ is the reduced frequency for model), the forced vibration frequency $f_m$ should be set at 12.5–156.25 Hz (Table 3). With regard to the limitation of forced vibration equipment used in the wind tunnel experiment, the forced vibration frequency cannot be set as large as this. Therefore, it is necessary to use LES to examine the characteristics of unsteady aerodynamic forces in a wider range of reduced frequency. For the LES, we change the forced vibration frequency from 0 to 160 Hz and the range of reduced frequency of vibration is from 0 to 2.5, as shown in Table 2.

**Table 2 Computational parameters**

| Parameter | Value |
|---|---|
| Wind speed, $U_H$ (m/s) | 5 |
| Forced vibration amplitude, $x_0$ (mm) | 4 |
| Rise/span ratio, $r/L$ | 0.15, 0.20, 0.25 |
| Forced vibration frequency, $f_m$ (Hz) | 0–160<br>(interval 10 Hz) |
| Reduced frequency of vibration, $f_m^*$ | 0–2.5 |

**Table 3 Determination of forced vibration frequency**

| | |
|---|---|
| 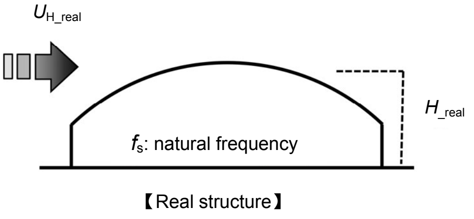 【Real structure】 | 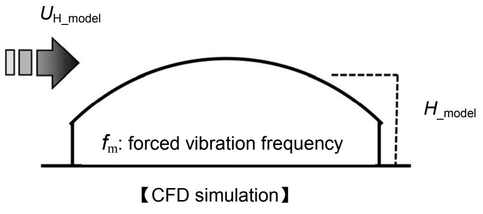 【CFD simulation】 |
| $f_{\_r}^* = \frac{f_s H_{\_r}}{U_{H\_r}}$<br>Mean roof height for real structure, $H_{\_r}$=20 m<br>Wind speed at mean roof height, $U_{H\_r}$=20–40 m/s<br>Natural frequency, $f_s$=0.4–2.5 Hz<br>Reduced frequency for real roof, $f_{\_r}^*$=0.2–2.5 | $f_m^* = \frac{f_m H}{U_H}$<br>Mean roof height for model, $H$=0.08 m<br>Wind speed at mean roof height, $U_H$=5 m/s<br>Forced vibration frequency, $f_m$=12.5–156.25 Hz<br>Reduced frequency for model, $f_m^*=f_{\_r}^*$=0.2–2.5 |

The computational domain is shown in Fig. 8a. In the simulation, various types of mesh arrangements were calculated. We compared the results of LES with those of the wind tunnel experiment. Then the mesh arrangement was selected which leads to results most corresponding with those of experiment, as shown in Fig. 8b. Two-dimensional flow is simulated in the same manner as in the wind tunnel experiment. The model is forced to vibrate in the first anti-symmetric mode using the dynamic mesh technique.

The computational and boundary conditions are summarized in Table 4. The governing equations are discretized based on the finite volume method. A central difference scheme for the convective term is used. The pressure implicit with splitting of operator (PISO) method is adopted to solve the discretized equation. The first-order Euler implicit is used as the time differential scheme (Ono *et al*., 2008; Lu *et al*., 2012).

### 3.2 Wind simulation

As is known, the flow around a structure is strongly affected by flow turbulence. Therefore, the proper generation of the inflow turbulence for the LES is essential in the determination of wind loads on structures. At present, several techniques have been developed. In general, there are three kinds of inflow turbulence generation methods. The first approach is to store the time history of velocity fluctuations obtained from a preliminary LES computation. Nozu and Tamura (1998) employed the interpolation method with the periodic boundary condition to simulate a fully developed turbulent boundary layer and tried to change the turbulent characteristics using roughness blocks. Another approach is to numerically simulate turbulent flow in auxiliary computational domains (often called a driver region set at the upstream region of a main computational domain). Lund *et al*. (1998) proposed the method to generate turbulent inflow data for the LES of a spatially developing boundary layer. Kataoka and Mizuno (1999) simplified Lund's method by assuming that the boundary layer thickness is constant within the driver region, and only the fluctuating part of velocity is recycled in the streamwise direction. Nozawa and Tamura (2001) and Chikamatsu *et al*. (2002) discussed the potential of LES for predicting turbulence characteristics in a

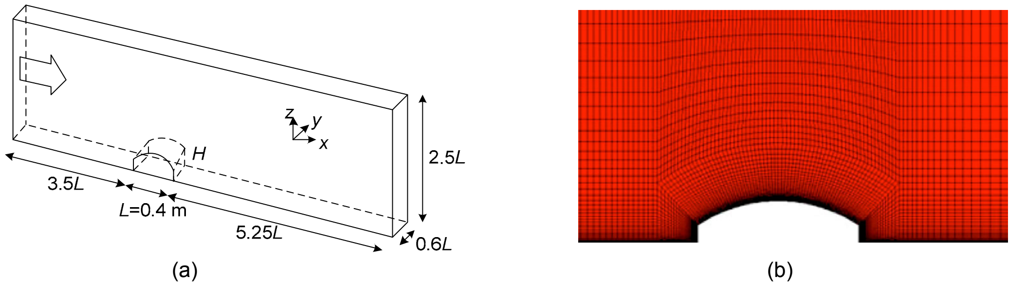

**Fig. 8 Computational domain (a) and mesh arrangement around roof (b)**

**Table 4 Computational and boundary conditions**

| Item | Description |
|---|---|
| Computational domain | $9.75L(x)\times0.6L(y)\times2.5L(z)$ |
| Inlet boundary | Inflow turbulence generated in preliminary computational domain |
| Upper boundary | Zero normal velocity and zero normal gradients of other variables |
| Side boundary | Cyclic boundary conditions |
| Outlet boundary | Zero normal gradients of all variables |
| Floor and model surfaces | No-slip condition |
| Grid discretization | $260(x)\times24(y)\times64(z)$=(399, 360) |
| Convection schemes | Second-order centered difference scheme |
| Time differential schemes | Euler implicit |
| Numerical algorithm | PISO algorithm |
| Time | $T$=4 s; $\Delta T=2.0\times10^{-4}$ s (Courant number: $9.1\times10^{-2}$) |

spatially developed turbulent boundary layer over a rough ground surface and improved Lund's method. The third approach is to use artificial numerical models to generate inflow turbulence statistically (Kondo *et al.*, 1997; Huang *et al.*, 2010; Yan and Li, 2015).

In this study, we use a preliminary LES to simulate inflow turbulence and store the time history of velocity fluctuations. Fig. 9 shows a schematic illustration of the domain of the preliminary computation. In the domain, the roughness blocks with heights of 3 cm, 5 cm, and 8 cm are distributed on the ground to generate turbulence. The computational and boundary conditions are summarized in Table 5. The periodic boundary condition is used at the inlet and outlet boundaries. The pressure gradient ($\Delta p$) is added to the inlet boundary, which influences the magnitude of velocity and structure of vortex (Nozu and Tamura, 1998).

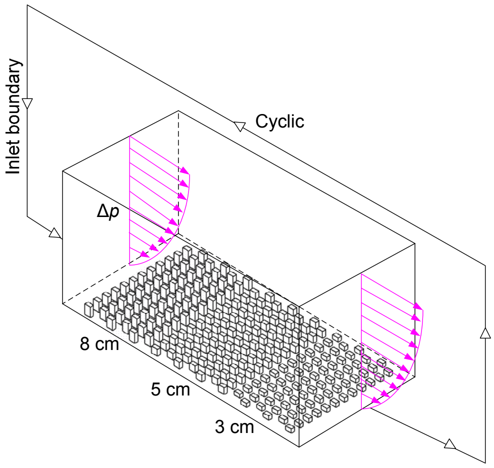

**Fig. 9 Preliminary computational domain**

The profiles of the mean wind speed and turbulent intensity at the inlet of the computational domain are shown in Fig. 10a. The longitudinal velocity spectrum at a height of $H$=90 mm is shown in Fig. 10b. In both figures the results of wind tunnel flow are also plotted for comparative purposes. It can be seen that the inflow turbulence used in the LES is

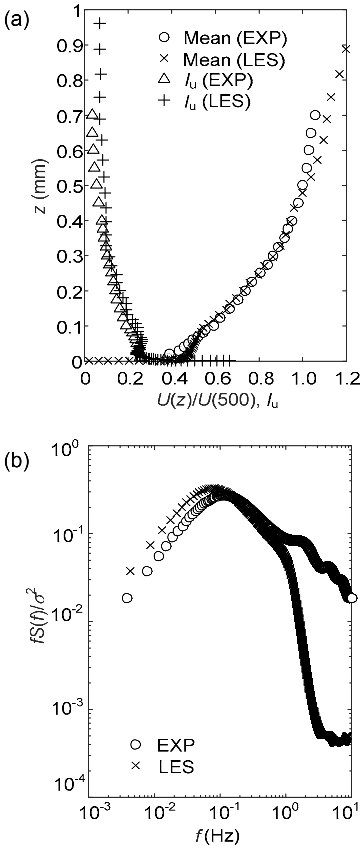

**Fig. 10 Comparison of inflow turbulence between wind tunnel experiment (EXP) and LES**

(a) Profiles of mean wind speed $U(z)$ and turbulence intensity $I_u$; (b) Longitudinal velocity spectrum $fS(f)/\sigma^2$ ($H$=90 mm)

**Table 5 Computational conditions for preliminary computation**

| Item | Description |
|---|---|
| Inlet boundary | Cyclic boundary condition |
| Upper boundary | Zero normal velocity and zero normal gradients of other variables |
| Side boundary | Cyclic boundary conditions |
| Outlet boundary | Cyclic boundary conditions |
| Floor and surfaces of roughness blocks | No-slip condition |
| Convection schemes | Monotone advanced and reconstruction scheme (MARS) method |
| Diffusion schemes | Centered difference scheme |
| Time differential schemes | 1st order Euler implicit |
| Numerical algorithm | PISO algorithm |
| Time step | $\Delta t$=2.0×10$^{-4}$ s |

generally in good agreement with that used in the wind tunnel experiment.

## 4 Results and discussion

### 4.1 Comparison with the wind tunnel experiment

In order to validate the LES computation, the distributions of the mean wind pressure coefficient $Cp_{\mathrm{mean}}$ and fluctuating wind pressure coefficient $Cp_{\mathrm{rms}}$ along the centerline of the vibrating roof are compared with those obtained from the wind tunnel experiment. Fig. 11 shows the results, in which the results for the frequencies of 0, 10, and 15 Hz are plotted. It can be seen that there is a generally good agreement between the LES and the wind tunnel experiment. In Fig. 11a, the difference is somewhat larger near the rooftop; the LES values are approximately 10% larger in magnitude than the experimental ones. This difference may be due to a difference in surface roughness of the roof between the LES and the wind tunnel experiment. In Fig. 11b, when $f_{\mathrm{m}}$=0 Hz, the value of $Cp_{\mathrm{rms}}$ for the LES is larger than that for the wind tunnel test. That may be because that the turbulence intensity of inflow turbulence used in the LES is slightly larger than that used in the wind tunnel test (Fig. 10).

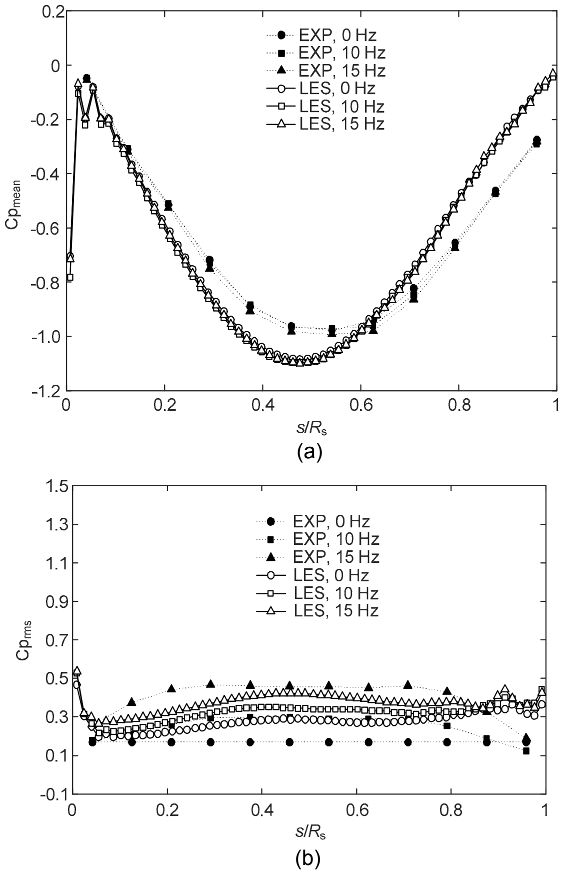

**Fig. 11 Comparisons for the distribution of the mean and fluctuating wind pressure coefficients along the centerline between LES and wind tunnel experiment**

(a) Mean wind pressure coefficients; (b) RMS fluctuating wind pressure coefficients

### 4.2 Distribution of wind pressures on the roof

The distributions of mean and RMS fluctuating wind pressure coefficients for various forced vibration frequencies are shown in Fig. 12. It can be seen that the mean wind pressure coefficients $Cp_{\mathrm{mean}}$ near the rooftop increase in magnitude and the RMS fluctuating wind pressure coefficients $Cp_{\mathrm{rms}}$ generally increase as the forced-vibration frequency increases. The variation is significant near the position of the greatest forced-vibration amplitude. These results indicate that the wind pressure field around the vibrating roof is strongly influenced by the vibration of the roof.

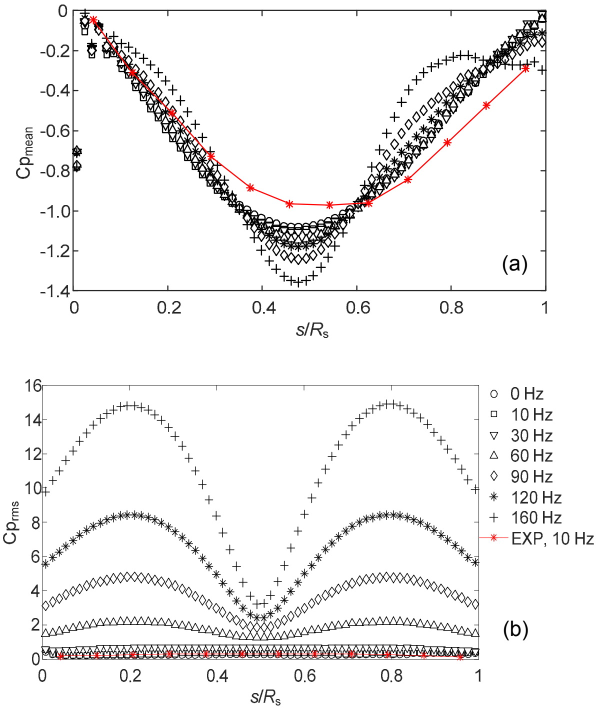

**Fig. 12 Variation of mean and fluctuating wind pressure coefficients with forced vibration frequency ($r/L$=0.15)**

(a) Mean wind pressure coefficients; (b) RMS fluctuating wind pressure coefficients

Fig. 13 shows the variations of mean and RMS fluctuating wind pressure coefficients with the rise/span ratio. It can be seen that the $Cp_{mean}$ changes from negative to positive at the leading edge of the roof as the rise/span ratio increases. Furthermore, the negative peak value increases in magnitude with an increase in rise/span ratio. The value of $Cp_{rms}$ increases with an increase in rise/span ratio at the middle part of the roof. However, the effect of $r/L$ on $Cp_{rms}$ is less significant than that on $Cp_{mean}$.

### 4.3 Discussion on flow field around the roof

The roof configurations at several steps (phases) during one period of vibration are shown in Fig. 14. The deformation of the windward side is upward and becomes the greatest at Step 2, and that of the leeward side is upward and becomes the greatest at Step 4.

Fig. 15 shows representative flow fields around a stationary or vibrating roof at a frequency of 10 Hz or 20 Hz. It can be seen that the wind speed increases near the roof regardless of the roof's vibration. In the case of a stationary roof ($f_m$=0 Hz), the flow separates near the 3/4 position of the roof from the leading edge. On the other hand, in the case of a vibrating roof, the separated vortex seems smaller than that in the stationary roof case, which may be owing to the vibration of the roof that restrains the separation of the vortex. In addition, the separated position at the rear of roof changes with the vibration of the roof. The separated position is relatively forward when the roof is vibrated in Step 1 to Step 3, because the deformation at the windward side of the roof makes the flow separated in advance. On the other hand, the separated position is relatively backward when the roof is vibrated in Step 3 to Step 5, with the result that the deformation at the leeward side of roof restrains the separated flow.

Fig. 16 shows the effect of the rise/span ratio on the flow field around a vibrating roof at a forced vibration frequency of 20 Hz. It can be seen that the wind speed near the rooftop becomes higher, generating larger suction as the rise/span ratio increases. Therefore, the negative peak value of $Cp_{mean}$ increases with an increase in rise/span ratio (Fig. 13). Furthermore, as the rise/span ratio increases, the vortex to the rear of the roof becomes larger.

### 4.4 Evaluation of unsteady aerodynamic forces

Fig. 17 (p.804) shows the aerodynamic stiffness and damping coefficients, $a_K$ and $a_C$, obtained from the LES and the wind tunnel experiment, plotted as a function of the reduced frequency of vibration $f_m^*$ ($f_m^*=f_mH/U_H$). The wind tunnel experiment was carried out over a limited range of $f_m^*$, while the LES was conducted over a wider range of $f_m^*$. It can be seen that the LES results are consistent with those of the

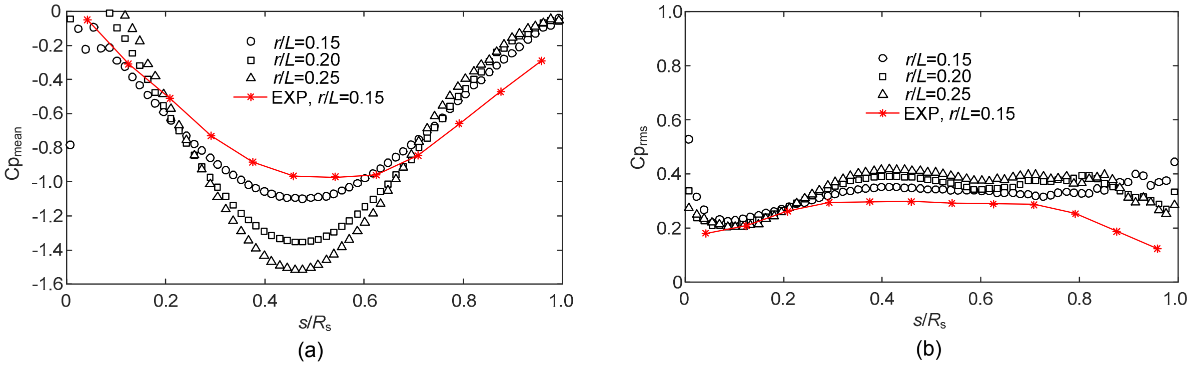

**Fig. 13 Variation of mean and fluctuating wind pressure coefficient with rise/span ratio ($f_m$=10 Hz)**
(a) Mean wind pressure coefficients; (b) RMS fluctuating wind pressure coefficients

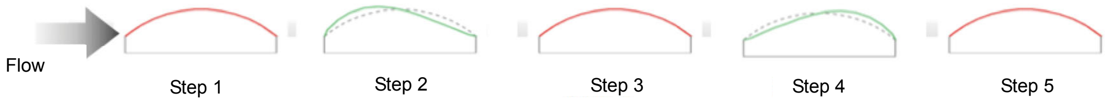

**Fig. 14 Roof configurations at several steps**

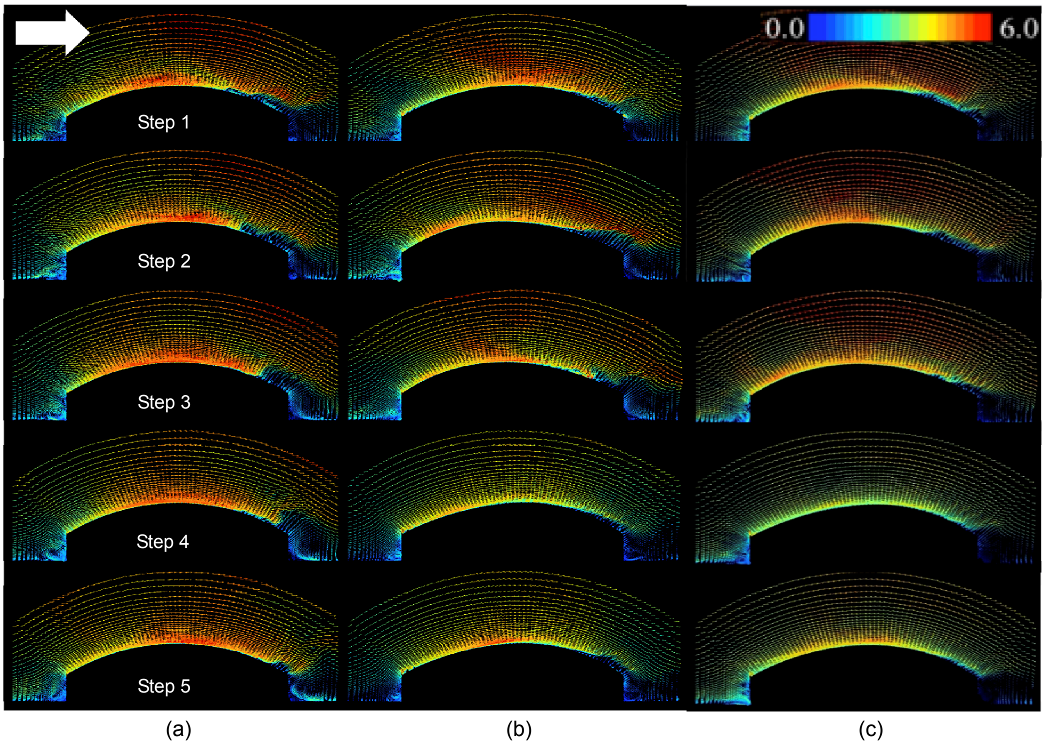

**Fig. 15 Flow fields (wind speed, m/s) around the roof for various forced vibration frequencies ($r/L$=0.15)**
(a) $f_m$=0 Hz; (b) $f_m$=10 Hz; (c) $f_m$=20 Hz

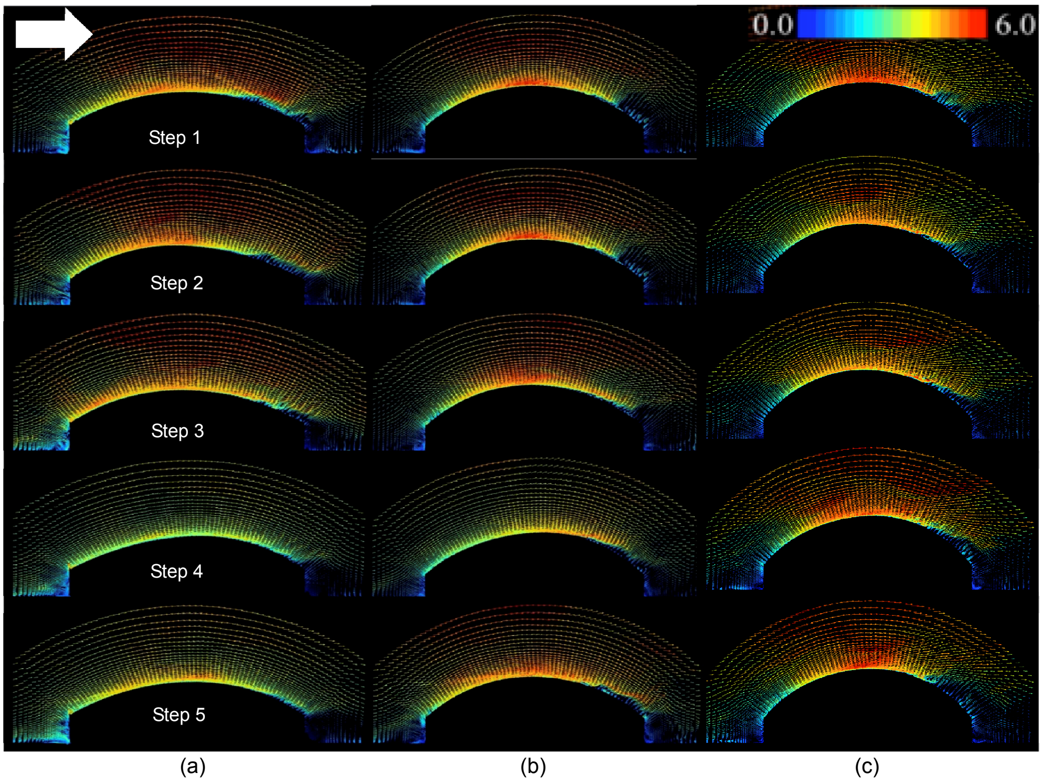

**Fig. 16 Flow fields (wind speed, m/s) around the roof for various rise/span ratios ($f_m$=20 Hz)**
(a) $r/L$=0.15; (b) $r/L$=0.20; (c) $r/L$=0.25

wind tunnel experiment, which indicates that the LES model can be used for investigating the characteristics of unsteady aerodynamic forces. The aerodynamic stiffness coefficient $a_\mathrm{K}$ is generally positive and increases with an increase in $f_\mathrm{m}^*$, which decreases the total stiffness of the system. On the other hand, the aerodynamic damping coefficient $a_\mathrm{C}$ is negative and increases in magnitude with an increase in $f_\mathrm{m}^*$, resulting in an increase in the total damping of the system.

The distribution of aerodynamic stiffness and damping coefficients $a_\mathrm{K}$ and $a_\mathrm{C}$ with $f_\mathrm{m}^*$ for various rise/span ratios is shown in Fig. 18. It can be seen that the values of $a_\mathrm{K}$ for $r/L$=0.15, 0.20, and 0.25 are generally consistent with each other when $f_\mathrm{m}^*$<0.4. However, when $f_\mathrm{m}^*$>0.4, the value of $a_\mathrm{K}$ decreases with an increase in the rise/span ratio. As for $a_\mathrm{C}$, the results for various rise/span ratios are generally similar to each other. Fig. 18 indicates that the value of $a_\mathrm{K}$ is influenced by the rise/span ratio of a long-span vaulted roof. However, the effect of the rise/span ratio on the value of $a_\mathrm{C}$ is small.

## 5 Conclusions

The unsteady aerodynamic behavior for long-span vaulted roofs has been investigated based on a wind tunnel experiment as well as with a numerical simulation (LES). A forced vibration test was carried out. First, the influence of a roof's vibration on the wind pressure was investigated. It is found that the

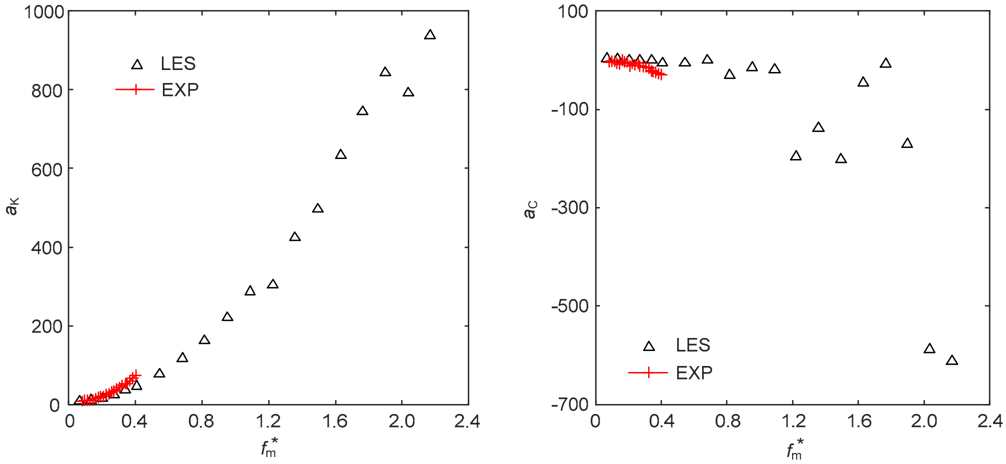

**Fig. 17 Comparisons of the LES and the wind tunnel experiment for the aerodynamic stiffness coefficient $a_\mathrm{K}$ and aerodynamic damping coefficient $a_\mathrm{C}$ versus reduced frequency of vibration $f_\mathrm{m}^*$**

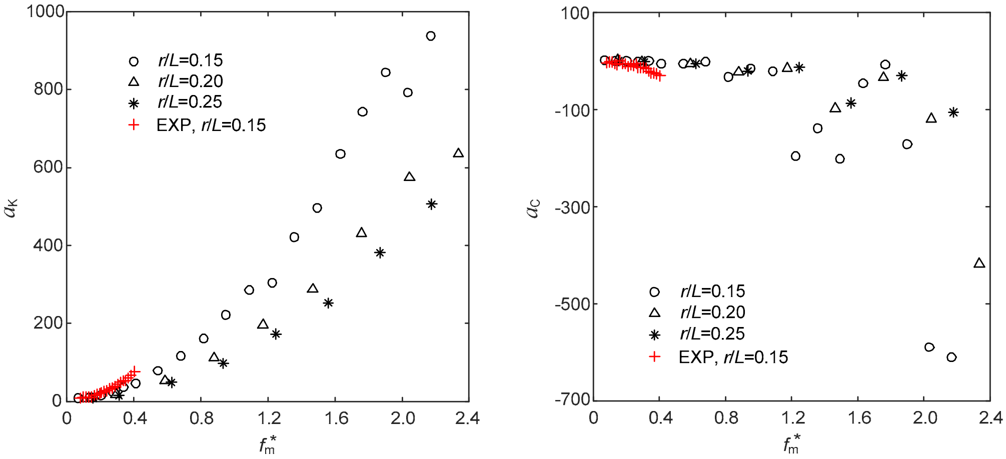

**Fig. 18 Aerodynamic stiffness coefficient $a_\mathrm{K}$ and aerodynamic damping coefficient $a_\mathrm{C}$ versus $f_\mathrm{m}^*$ for different rise/span ratio $r/L$**

wind pressure on a vibrating roof is strongly influenced by the roof's vibration. The flow field around a vibrating roof was also investigated. It is found that the vibration of the roof may restrain the separation of a vortex near the trailing edge of the roof. Finally, the characteristics of unsteady aerodynamic force acting on a long-span vaulted roof were evaluated. Both the wind tunnel experiment and CFD simulation show similar results for the variation of aerodynamic stiffness and damping coefficients $a_K$ and $a_C$ with reduced frequency of vibration $f_m^*$, which implies that the LES is effective for the investigation of the characteristics of unsteady aerodynamic forces. The aerodynamic stiffness coefficient is generally positive, which decreases the total stiffness of the system, resulting in aeroelastic instability of long-span vaulted roofs with lower stiffness. On the other hand, the aerodynamic damping coefficient is negative, which results in an increase in the total damping of the system, resulting in a decrease in the response of the roof. Therefore, it is necessary to consider the effects of unsteady aerodynamic forces in the wind-resistant design of long-span vaulted roof with lightweight and low stiffness to evaluate the response of the roof more reasonably.

## References

Blackmore, P.A., Tsokri, E., 2006. Wind loads on curved roof. *Journal of Wind Engineering and Industrial Aerodynamics*, **94**(11):833-844. http://dx.doi.org/10.1016/j.jweia.2006.06.006

Chen, F.B., Li, Q.S., Wu, J.R., *et al*., 2011. Wind effects on a long-span beam string roof structure: wind tunnel test, field measurement and numerical analysis. *Journal of Constructional Steel Research*, **67**(10):1591-1604. http://dx.doi.org/10.1016/j.jcsr.2011.04.003

Chen, Z.Q., Wu, Y., Sun, X.Y., 2015. Research on the added mass of open-type one-way tensioned membrane structure in uniform flow. *Journal of Wind Engineering and Industrial Aerodynamics*, **137**:69-77. http://dx.doi.org/10.1016/j.jweia.2014.12.004

Chikamatsu, A., Nozawa, K., Tamura, T., 2002. Large eddy simulation of turbulent flows around a cube in an imitated atmospheric boundary layer. The 17th National Symposium on Wind Engineering (in Japanese).

Daw, D.J., Davenport, A.G., 1989. Aerodynamic damping and stiffness of a semi-circular roof in turbulent wind. *Journal of Wind Engineering and Industrial Aerodynamics*, **32**(1-2):83-92. http://dx.doi.org/10.1016/0167-6105(89)90019-6

Huang, S.H., Li, Q.S., Wu, J.R., 2010. A general inflow turbulence generator for large eddy simulation. *Journal of Wind Engineering and Industrial Aerodynamics*, **98**(10-11): 600-617. http://dx.doi.org/10.1016/j.jweia.2010.06.002

Katagiri, J., Ohkuma, T., Marukawa, H., 2001. Motion-induced wind forces acting on rectangular high-rise buildings with side ratio of 2. *Journal of Wind Engineering and Industrial Aerodynamics*, **89**(14-15):1421-1432. http://dx.doi.org/10.1016/S0167-6105(01)00148-9

Kataoka, H., Mizuno, M., 1999. Numerical flow computation around 3D square cylinder using inflow turbulence. *Journal of Architecture and Planning (Transactions of AIJ)*, **64**(523):71-77 (in Japanese). http://dx.doi.org/10.3130/aija.64.71

Kondo, K., Murakami, S., Mochida, A., 1997. Generation of velocity fluctuations for inflow boundary condition of LES. *Journal of Wind Engineering and Industrial Aerodynamics*, **67-68**:51-64. http://dx.doi.org/10.1016/S0167-6105(97)00062-7

Lu, C.L., Li, Q.S., Huang, S.H., *et al*., 2012. Large eddy simulation of wind effects on a long-span complex roof structure. *Journal of Wind Engineering and Industrial Aerodynamics*, **100**(1):1-18. http://dx.doi.org/10.1016/j.jweia.2011.10.006

Lund, T.S., Wu, X., Squires, K.D., 1998. Generation of turbulent inflow data for spatially-developing boundary layer simulations. *Journal of Computational Physics*, **140**(2):233-258. http://dx.doi.org/10.1006/jcph.1998.5882

Natalini, M.B., Morel, C., Natalini, B., 2013. Mean loads on vaulted canopy roofs. *Journal of Wind Engineering and Industrial Aerodynamics*, **119**:102-113. http://dx.doi.org/10.1016/j.jweia.2013.05.001

Nozawa, K., Tamura, T., 2001. Large eddy simulation of a turbulent boundary layer over a rough ground surface and evaluation of its fluctuating velocity profile. *Journal of Structural and Construction Engineering (Transactions of AIJ)*, **66**(541):87-94 (in Japanese). http://dx.doi.org/10.3130/aijs.66.87_3

Nozu, T., Tamura, T., 1998. Generation of unsteady wind data in boundary layers and its turbulence structures. The 15th National Symposium on Wind Engineering (in Japanese).

Ohkuma, T., Marukawa, H., 1990. Mechanism of aeroelastically unstable vibration of large span roof. *Wind Engineers, JAWE*, **1990**(42):35-42 (in Japanese). http://dx.doi.org/10.5359/jawe.1990.35

Ono, Y., Tamura, T., Kataoka, H., 2008. LES analysis of unsteady characteristics of conical vortex on a flat roof. *Journal of Wind Engineering and Industrial Aerodynamics*, **96**(10-11):2007-2018. http://dx.doi.org/10.1016/j.jweia.2008.02.021

Uematsu, Y., Uchiyama, K., 1982. Wind-induced dynamic behaviour of suspended roofs. *The Technology Reports of the Tohoku University*, **47**:243-261.

Wu, Y., Chen, Z.Q., Sun, X.Y., 2015. Research on the wind-induced aero-elastic response of closed-type saddle-shaped

tensioned membrane models. *Journal of Zhejiang University-SCIENCE A (Applied Physics & Engineering)*, **16**(8):656-668.
http://dx.doi.org/10.1631/jzus.A1400340

Yan, B.W., Li, Q.S., 2015. Inflow turbulence generation methods with large eddy simulation for wind effects on tall buildings. *Computers & Fluids*, **116**:158-175.
http://dx.doi.org/10.1016/j.compfluid.2015.04.020

Yang, Q.S., Wu, Y., Zhu, W.L., 2010. Experimental study on interaction between membrane structures and wind environment. *Earthquake Engineering and Engineering Vibration*, **9**(4):523-532.
http://dx.doi.org/10.1007/s11803-010-0034-0

## 中文概要

**题　目：基于大涡模拟方法研究大跨度曲面屋盖非定常气动力的特性**

**目　的：** 探讨作用于大跨度曲面屋盖非定常气动力的特性，为考虑非定常气动力影响的大跨度曲面屋盖抗风设计提供理论参考。

**创新点：** 1. 采用强迫振动试验；2. 采用大涡模拟（LES）流入脉动风的生成方法；3. 研究大跨度曲面屋盖非定常气动力特性。

**方　法：** 1. 通过强迫振动风洞试验方法探讨风速、强迫振动振幅、屋盖的矢跨比和缩减频率对非定常气动力的影响；2. 采用计算流体力学数值模拟重现风洞试验，从而在更宽的缩减频率范围内分析非定常气动力的特性，并且通过可视化流场的分析探讨风与屋盖相互作用的机理。

**结　论：** 1. 屋盖的振动对屋盖表面的风压分布影响较大。2. 屋盖的振动可能抑制屋盖背风面漩涡的脱落。3. 根据风洞试验和数值模拟的结果分析得到的矢跨比、风速和振动振幅对气动阻尼系数和气动刚度系数的影响较小；气动阻尼系数和气动刚度系数主要随着缩减频率的变化而变化。4. 气动刚度系数为正值，使得结构的总刚度减小，从而减小结构的固有频率；气动阻尼系数为负值，使得结构总阻尼增加。5. 风洞试验和 LES 模拟结果的一致性可以说明，LES 是一个能够有效研究非定常气动力特性的数值模拟方法。

**关键词：** 大涡模拟；大跨度曲面屋盖；非定常气动力；风洞试验；强迫振动试验